Pr_6O_{11} clusters anchored CoFe-LDH on vertical graphene nanosheets as oxygen evolution electrocatalyst for long-term high-current-density seawater electrolysis

Quan Wu[1, 2], Xiaoyu Dong[1], Kefeng Ouyang[1], Youfa Liu[1], Hao Lei[1], Jie Yu[1, 2*], Yan Huang[1*]

1 School of Material Science and Engineering, Harbin Institute of Technology, Shenzhen, University Town, Shenzhen 518055, China.

2 Guangdong Provincial Key Laboratory of Semiconductor Optoelectronic Materials and Intelligent Photonic Systems, Shenzhen Engineering Lab for Supercapacitor Materials, Harbin Institute of Technology, Shenzhen, University Town, Shenzhen 518055, China.

Experimental Section

***Materials*:** Graphite plate (GP) was provided by Kunshan Xinghengchang Co., Ltd. $Fe(NO_3)_2 \cdot 9H_2O$ (99.9%), $Co(NO_3)_2 \cdot 6H_2O$ (99%), RuO_2 (99.9%), K_2SO_4 (99%), KOH (99.99%) and Platinum on carbon catalyst (20 wt.% Pt) were acquired from Shanghai Macklin Biochemical Co., Ltd. $Pr(NO_3)_3 \cdot 6H_2O$ (99%) and concentrated hydrochloric acid (37 wt.%) were purchased from Shanghai Aladdin Reagent Co., Ltd. Anhydrous ethanol (99.7%) was obtained from Sichuan Xilong Scientific Co., Ltd. Self-made deionized water from the laboratory was used in the experiment. Natural seawater was used directly without any additional treatment, extracted from Shenzhen Bay, South China Sea. Nafion solution (composition of 5 wt.% Nafion, 45 wt.% water and 50 wt.% volatile organic compounds) was supplied by Suzhou Sinero Technology Co., Ltd. High purity argon (99.99%) was purchased from Shenzhen Shente Industrial Gas Co., Ltd. CH_4 (99.99%) and H_2 (99.99%) were provided by Guangzhou Xiangyuan Industrial Gas Co., Ltd.

***Preparation of GP/VGSs*:** Prior to synthesis, pristine GP was ultrasonically cleaned in 1 M HCl and ethanol. GP was put into ceramic crucible and heated by a tube furnace from room temperature to 1100 °C at a heating speed of 10 °C/min with full Ar flow. Afterward, the system was held at 1100 °C for 4 h under CH_4 and H_2 (gas flow ratio was controlled at 1:5) mixture atmosphere. Then, the tube furnace stopped heating with natural cooling in the Ar atmosphere. The product (GP/VGSs) was obtained at ambient temperature.

***Preparation of GP/VGSs-CoFe layered double hydroxides (LDH)-Pr_6O_{11}*:** The preparation of GP/VGSs-CoFe LDH-Pr_6O_{11} was operated by a typical electrochemical deposition. The electrolyte was made up of nitrate solution of 3.2 mmol $Co(NO_3)_2 \cdot 6H_2O$, 0.72 mmol $Fe(NO_3)_2 \cdot 9H_2O$, 0.08 mmol $Pr(NO_3)_3 \cdot 6H_2O$ and 80 mL water. In the electrodeposition process, a GP/VGSs sample (0.5 × 1 cm^2), a graphite rod and an Ag/AgCl electrode served as the working, the counter and the reference electrode, respectively. During the electrodeposition process, -1.0 V voltage was

applied to the three-electrode system in nitrate solution for 100 s. The obtained product was named as GP/VGSs-CoFe LDH-Pr_6O_{11}. For comparison, a similar electrodeposition was manipulated without Pr_6O_{11} clusters anchoring (Co:Fe molar ratios = 4:1) on a GP/VGSs substrate, and the corresponding product was named as GP/VGSs-CoFe LDH. Moreover, GP/VGSs-$Co(OH)_2$, GP/VGSs-$Fe(OH)_3$ and GP/VGSs-Pr_6O_{11} samples were prepared by 4 mmol $Co(NO_3)_2{\cdot}6H_2O$, $Fe(NO_3)_2{\cdot}9H_2O$, $Pr(NO_3)_3{\cdot}6H_2O$ in 80 mL water via the similar electrodeposition process, respectively. Furthermore, CoFe LDH-Pr_6O_{11} hybrid was prepared on GP (cleaning after 1 M HCl and ethanol) via similar electrodeposition process, named as GP-CoFe LDH-Pr_6O_{11}. The catalyst loading of the prepared samples averaged 1.74 mg/cm^2.

In this process, nitrate anions in the electrolyte are reduced to OH^-, increasing the local pH near the electrode, leading to the formation of metal (Co, Fe and Pr) hydroxides [1]. For Fe and Co, the hydroxides are stable in the local OH^- environment and tend to form LDH. However, rare-earth metal hydroxides continue to be oxidized by oxygen in the local OH^- environment, resulting in more stable rare-earth metal oxides [2, 3]. For Pr, the most stable oxide form in air is Pr_6O_{11} [4-6].

***Preparation of CoFe LDH-Pr_6O_{11}*:** The CoFe LDH-Pr_6O_{11} electrocatalyst powder was scraped off from the substrate of GP/VGSs (belong to GP/VGSs-CoFe LDH-Pr_6O_{11}) sample by knife.

***Characterization*:** The X-ray diffraction (XRD) was performed on a Rigaku Smartlab instrument via Cu Kα radiation source (wavenumbers = 1.5418 Å) at a scanning rate of 10°/min. The micro-morphologies of samples were taken on a HITACHI S-4800 field-emission scanning electron microscope (SEM). The transmission electron microscope (TEM) images were captured by a JEOL JEM-F200 system equipped with an energy dispersive spectrometer (EDS). The Raman spectroscopy was examined under an air ion laser with 532 nm wavenumbers by a Renishaw inVia equipment. The X-ray photoelectron spectroscopy (XPS) was detected for investigating the surface composition of samples using Al Kα radiation on ESCALAB 250 instrument. The Brunauer-Emmett-Teller (BET) experiments were recorded by micromeritics

ASAP 2460 analyzer after degassing treatment. The contact angle tests were carried out by a Dataphysics OCA 20 contact angle tester. For the TEM and XRD characterizations, the CoFe LDH-Pr_6O_{11} electrocatalyst powder was used to eliminate the influence of the thick carbon substrate.

***Electrochemical measurements*:** The electrochemical tests were performed on an electrochemical workstation (Biologic, VSP 300, current ranging to 1 A) with a standard three-electrode system at room temperature. In the three-electrode system, a catalysts-loaded GP or GP served as the working electrode, while Hg/HgO and graphite rod electrodes were used as the reference electrode and the counter electrode, respectively. Electrochemical experiments were performed in 1 M KOH solution for conventional freshwater tests, while the seawater experiments were examined in 1 M KOH/seawater solution or 1 M KOH/0.025 M K_2SO_4/seawater solution. Before OER testing excessive O_2 was introduced into the electrolyte solution to saturation. The reversible hydrogen electrode (RHE) was calibrated to all the potentials according to the equation of $E_{(RHE)} = E_{Hg/HgO} + 0.098 + 0.059$ pH. The polarization curves of OER were tested by linear sweep voltammetry (LSV) technique at a scan rate of 5 mV/s with 90% iR-compensation. The overpotentials (η) of OER were calculated by the following equations: η (V) = $E_{(RHE)}$ - 1.23 V. Cyclic voltammetry (CV) curves were recorded with different scan rates (20, 40, 60, 80, and 100 mV/s) in the non-faradaic range of 1.1 to 1.2 V (vs. RHE) and each ΔJ was calculated at 1.15 V (vs. RHE) for the further calculating the double-layer capacitance (C_{dl}) values. Electrochemically surface area (ECSA) = $(C_{dl} \times A)/C_s$, where A was the geometric area of electrode (0.5 cm^2 in our case) and C_s was the specific capacitance of a smooth sample under the same conditions (0.04 mF/cm^2 for LDH) [7, 8]. The chronopotentiometry tests were manipulated at different current density for evaluating the stability of catalysts. The electrochemical impedance spectroscopy (EIS) was collected at the fixed overpotential of 1.53 V (vs. RHE) in the frequency range from 10^{-2} Hz to 10^5 Hz with a certain amplitude of 5 mV. For comparative samples of precious metals catalysts, the homogeneous catalyst ink of 10 mg Pt/C or RuO_2, 50 μL of 5 wt.% Nafion solution, 190 μL ethanol, and 760 μL distilled water was prepared by ultrasonication

for 30 min and then 100 μL ink was dropped onto the surface of GP (GP: 0.5 × 1 cm^2, loading of noble-metal catalyst: 2 mg/cm^2). Especially, the overall water electrolysis test was carried out by an assembled two-electrode system of GP/VGSs-CoFe LDH-Pr_6O_{11} and the HER NiMoN sample, comparing to a system of Pt/C and RuO_2. The NiMoN sample was prepared according the previous reference [9].

The calculation of turnover frequency (TOF) value was based on the equation:

$$TOF = \frac{\text{number of } H_2 \text{ turnovers}}{\text{number of metal ions}} = \frac{j \times S \times N_A / (z \times F)}{ML \times S \times N_A \times \frac{\text{weight content of metal ion in electrocatalyst}}{\text{the molecular weight of metal}}}$$

In this equation, j represented the current density (A/cm^2) at a given overpotential (300 mV for OER in this work). S was the value of the surface area of electrode (cm^2) and N_A was Avogadro's number (6.02×10^{23} mol^{-1}). z was electron transfer number per molecule generated (for OER, z = 4). F meant the Faraday constant, which was 96485 C/mol. ML was the mass loading of electrocatalyst on electrode (g/cm^2). Weight content of metal ions in electrocatalyst was calculated by the feeding ratio of metal salt and the electrocatalyst loading. The molecular weight of metal is according to Fe = 55.9 mol/g, Co = 58.9 mol/g and Pr = 140.9 mol/g.

***DFT Calculation*:** Vienna Ab-initio Simulation Package (VASP) was performed for all density functional theory (DFT) calculations within the generalized gradient approximation by the Perdew-Burke-Ernzerhof functional [10]. The projected augmented wave potentials were chosen to describe the ionic cores and valence electrons were taken into account using a plane wave basis set with a kinetic energy cutoff of 450 eV. The DFT-D3 empirical correction method was employed to illustrate van der Waals interactions [11]. Geometry optimizations were operated with the force convergency smaller than 0.05 eV/Å. Gamma-centered scheme k-point of 1 × 1 × 1 was applied for all the surface calculations. Moreover, all the atoms were relaxed in all the calculations. The DFT+U approach was introduced to Fe and Co for treating the highly localized 3d states (parameters of U–J = 5.3 and 3.32 eV, respectively) [12, 13]. Furthermore, spin-polarization effect was also considered [14]. The

type of pseudopotential was POTCAR H, O, Fe, Co, Pr-3 and Cl. The Gibbs free energy changes (ΔG) of each elementary reaction step during OER were calculated using the computational hydrogen electrode (CHE) model [15]. In this model, the chemical potential was equal to the energy of half of the gas-phase H_2 at 0 V vs RHE. The electrode potential (U verse RHE) was taken into consideration by adding –eU when an electron transforming step occurred. That was G(U) = G (0 V) – n × e × U, where e was the elementary charge of an electron, n was the number of proton-electron pairs transferred, and U was the applied potential. The ΔG was calculated by the following equation [16]:

$$\Delta G = \Delta E + \Delta E_{ZPE} - T\Delta S$$

Where the value of ΔE, ΔE_{ZPE} and ΔS denoted the changes of DFT energy, the zero-point energy and the entropy at 298.15 K, respectively.

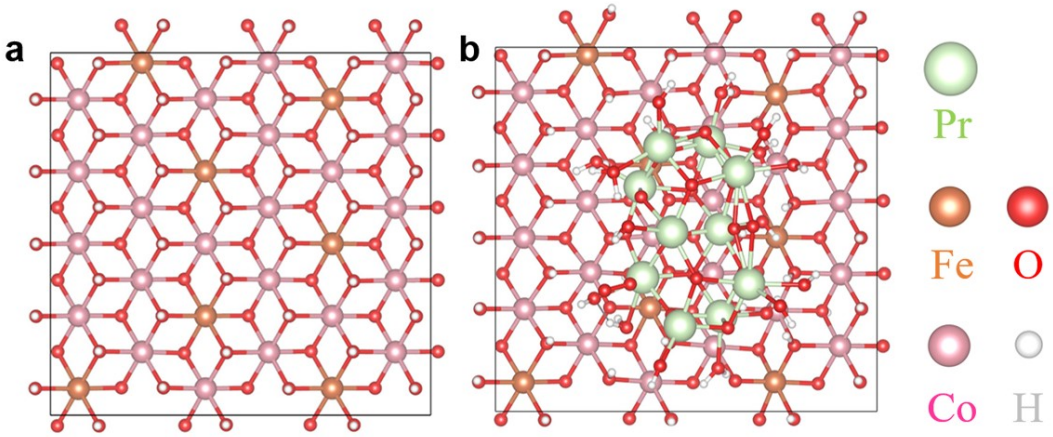

Figure S1. Optimized structure of (a) CoFe LDH and (b) CoFe LDH-Pr_6O_{11}.

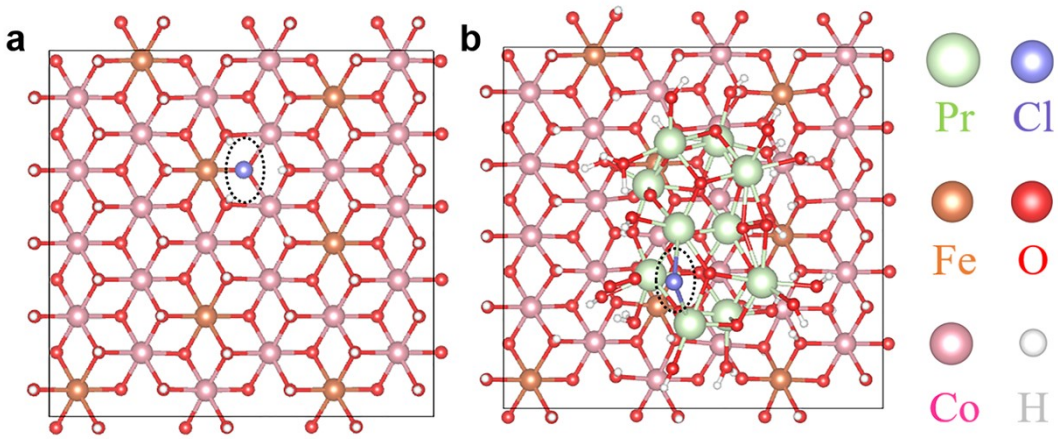

Figure S2. Model structure of (a) CoFe LDH and (b) CoFe LDH-Pr_6O_{11} for Cl adsorption.

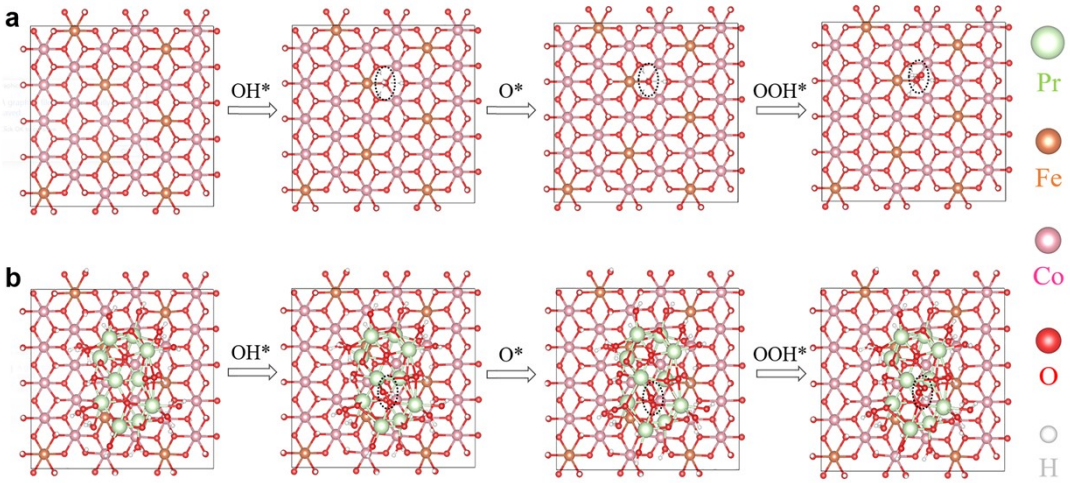

Figure S3. Model structures during OER process on (a) CoFe LDH and (b) CoFe LDH-Pr_6O_{11}.

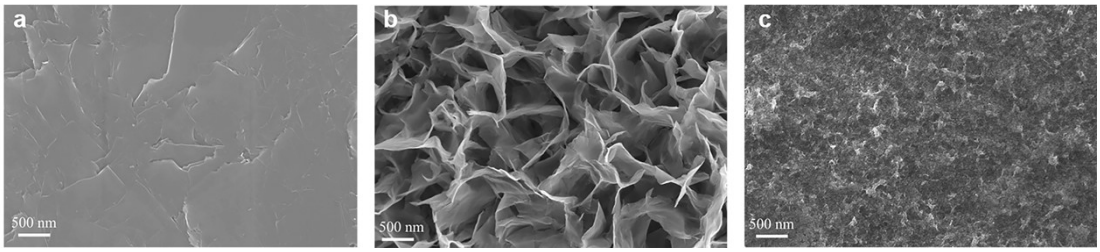

Figure S4. The SEM image of (a) GP; (b) GP/VGSs-CoFe LDH and (c) GP/VGSs-CoFe LDH-Pr_6O_{11}.

Compared to CoFe LDH, Pr_6O_{11} has relatively poorer crystallinity. The incorporation of Pr_6O_{11} increases the irregularity and defects in the layers during the crystallization process, thereby disrupting the nucleation and final crystallization of CoFe LDH during electrodeposition [17-19]. As a result, this leads to the formation of smaller size of CoFe LDH-Pr_6O_{11} nanosheets.

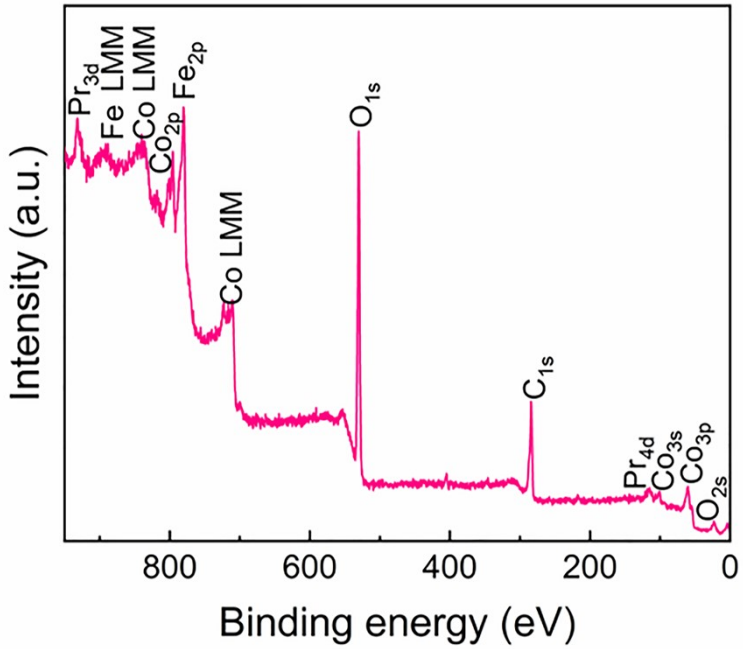

Figure S5. The XPS full spectrum of GP/VGSs-CoFe LDH-Pr_6O_{11}.

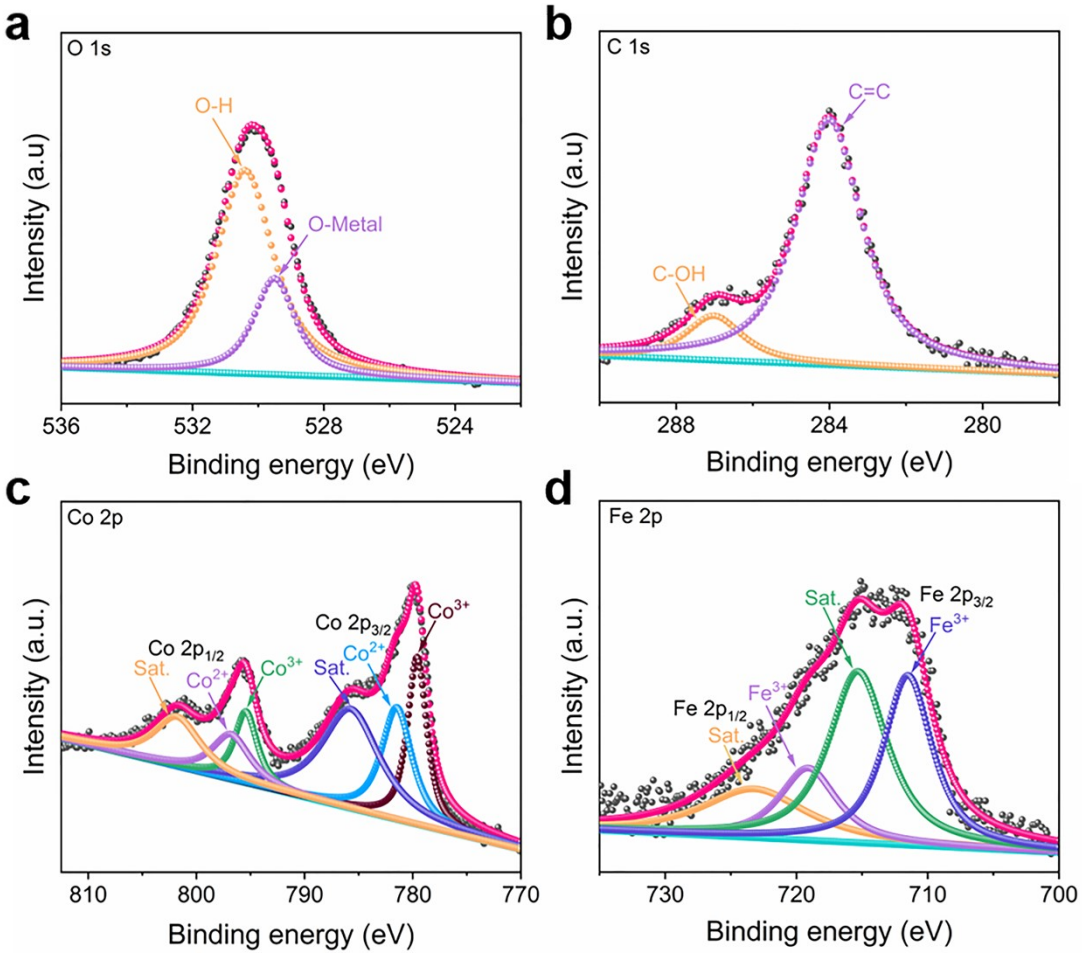

Figure S6. (a) O 1s; (b) C 1s; (c) Co 2p and (d) Fe 2p XPS spectra of GP/VGSs-CoFe LDH-Pr_6O_{11}.

For the O 1s spectrum (Figure S6a), the peak at 530.4 eV is assigned to O-H, and the peak at 529.5 eV is attributed to O-Metal [20]. As exhibited in Figure S6b, the peak at 287.0 eV corresponds to C-OH, and the peak at 284.0 eV matches to C=C [21]. As seen in Figure S6c, the Co 2p orbital is split into Co $2p_{1/2}$ (peaks at 801.8 eV, 796.8 eV, and 795.5 eV) and Co $2p_{3/2}$ (peaks at 785.8 eV, 781.5 eV, and 779.5 eV). Among these, the peaks at 801.8 eV and 785.8 eV, the peaks at 796.8 eV and 781.5 eV, and the peaks at 795.5 eV and 779.5 eV are generated by satellite peaks of Co, Co^{2+} and Co^{3+}, respectively [22, 23]. The two peaks at 723.2 eV and 715.3 eV are satellite vibration of Fe, while the peaks at 719.2 eV and 711.5 eV are ascribed to Fe^{3+} in the Fe 2p spectrum (Figure S6d) [24]. The Fe 2p orbital is also split into two sub-orbitals of Fe $2p_{1/2}$ (peaks of 723.2 eV and 719.2 eV) and Fe $2p_{3/2}$ (peaks of 715.3 eV and 711.5 eV).

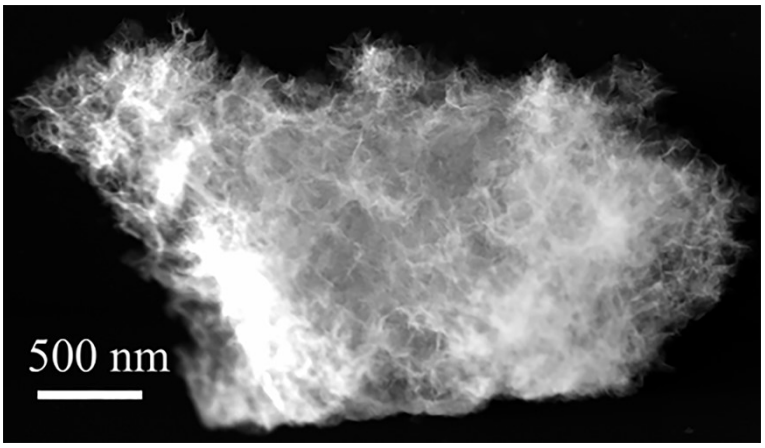

Figure S7. The high-angle annular dark field of TEM image of CoFe LDH-Pr_6O_{11}.

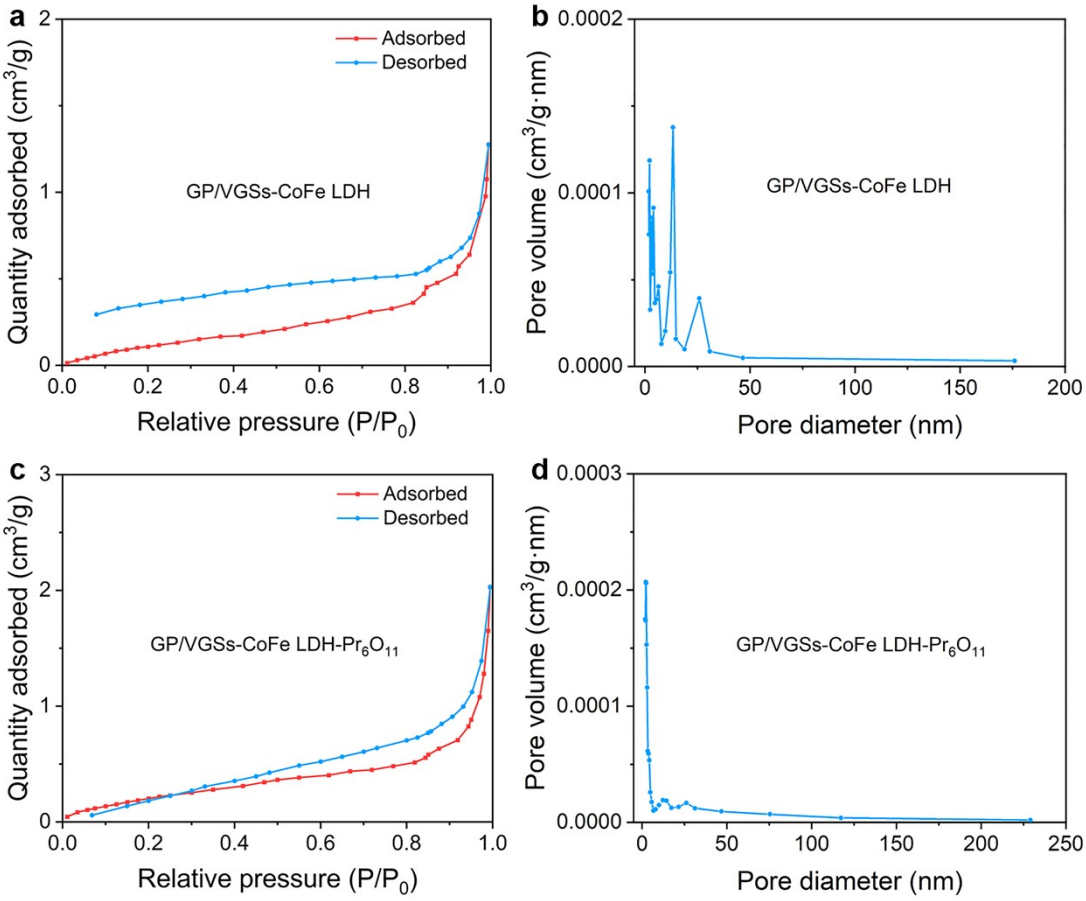

Figure S8. (a) The N_2 adsorption-desorption isotherm curve and (b) the pore size distribution plot of GP/VGSs-CoFe LDH; (c) The N_2 adsorption-desorption isotherm curve and (d) the pore size distribution plot of GP/VGSs-CoFe LDH-Pr_6O_{11}.

Due to the low specific surface area and the poor desorption of N_2 on the surface structure of GP/VGSs-CoFe LDH, the curve in Figure S8a does not fully close. For the pore size distribution of GP/VGSs-CoFe LDH (Figure S8b), a wide range of pore diameters from 2 to 15 nm can be observed. In contrast, the GP/VGSs-CoFe LDH-Pr_6O_{11} sample (Figure S8c) exhibits a type IV closed-loop curve, confirming its porous surface structure. For the pore size distribution of the GP/VGSs-CoFe LDH-Pr_6O_{11} sample (Figure S8d), the pore diameters are mainly concentrated in the 2-5 nm range, which correlates with the formation of smaller nanosheets structures on surface after the incorporation of Pr_6O_{11}.

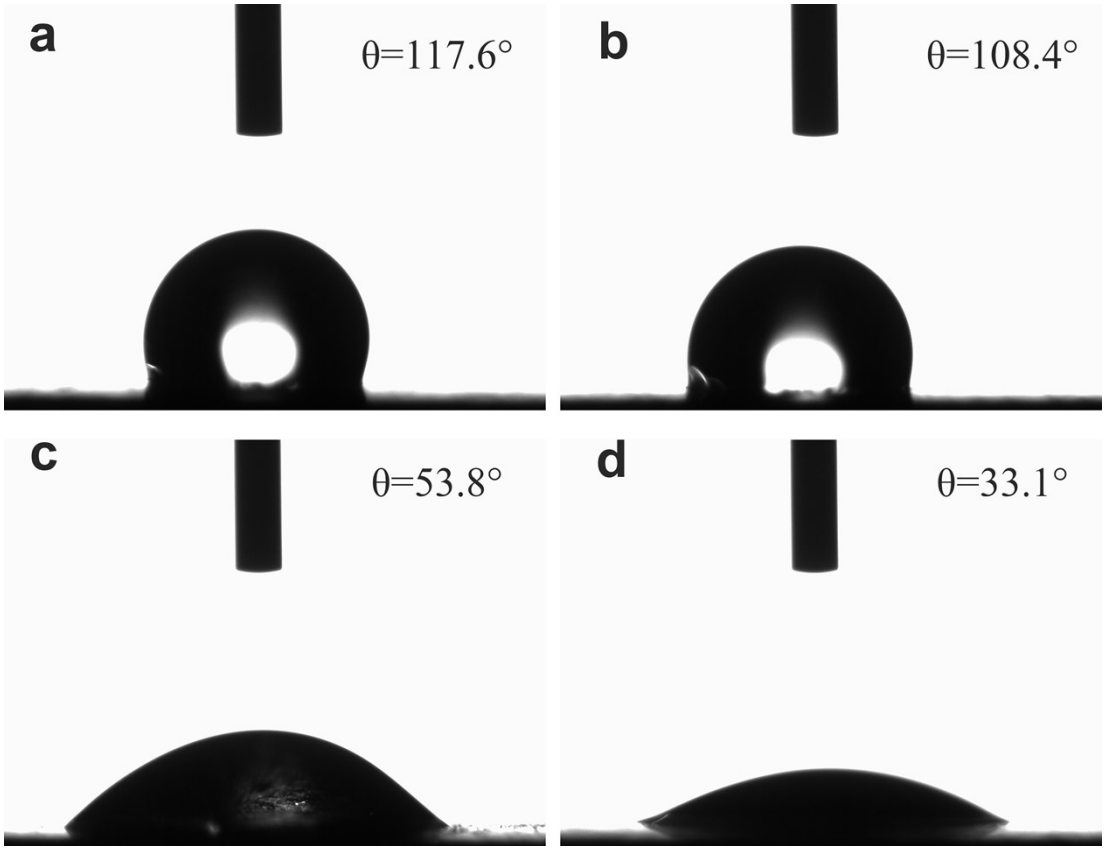

Figure S9. The contact angle image of (a) GP; (b) GP/VGSs; (c) GP/VGSs-CoFe LDH and (d) GP/VGSs-CoFe LDH-Pr_6O_{11}.

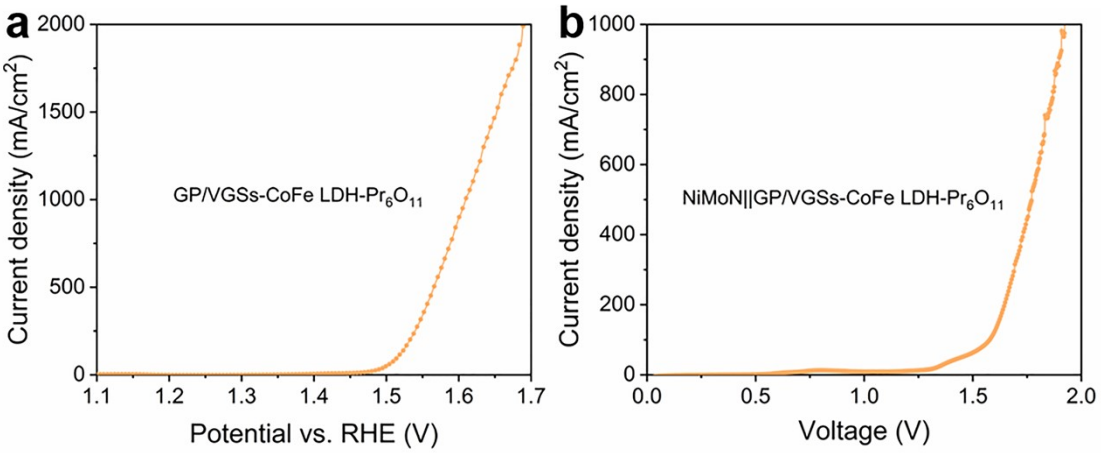

Figure S10. The LSV curves of (a) GP/VGSs-CoFe LDH-Pr_6O_{11} and (b) NiMoN||GP/VGSs-CoFe LDH-Pr_6O_{11} in 1 M KOH + seawater solution.

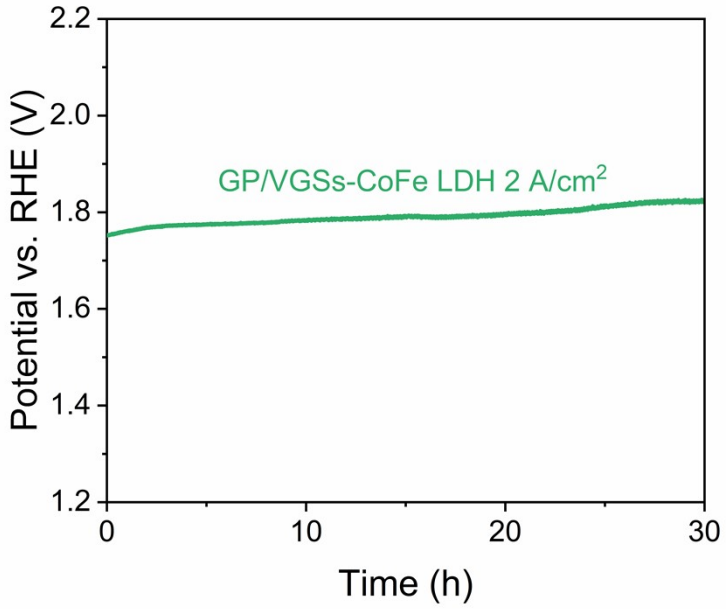

Figure S11. OER stability of GP/VGSs-CoFe LDH in 1 M KOH + 0.025 M K_2SO_4 + seawater.

As aforementioned in Figure 3b, the GP/VGSs-CoFe LDH-Pr_6O_{11} exhibits OER overpotential of 466 mV and OER stability for 70 h at 2 A/cm^2 in 1 M KOH + 0.025 M K_2SO_4 + seawater solution. Under the same electrolyte conditions, the OER stability of GP/VGSs-CoFe LDH demonstrates OER overpotential of 522 mV and a shorter lifespan of 30 h at the same current density of 2 A/cm^2 (Figure S11). By comparing Figure S11 with Figure 3b, we can conclude that the incorporation of Pr_6O_{11} indeed reduces the corrosion of the catalyst by Cl in experimental evidence due to the longer lifespan and the lower OER overpotential of GP/VGSs-CoFe LDH-Pr_6O_{11}.

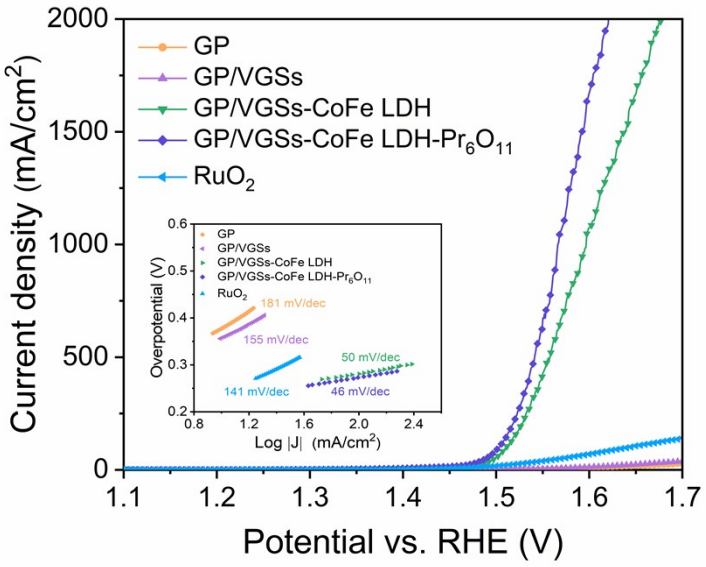

Figure S12. The LSV curves and the inset (Tafel plots) of GP, GP/VGSs, GP/VGSs-CoFe LDH, GP/VGSs-CoFe LDH-Pr_6O_{11} and RuO_2 in 1 M KOH solution.

As seen in Figure S12, the intrinsic OER activity of GP and GP/VGSs substrates is low (with poor Tafel slopes of 181 mV/dec and 155 mV/dec, respectively). When the catalyst is loaded onto the GP/VGSs substrate in the form of CoFe LDH, the OER performance is greatly improved (synergistic effect between Co and Fe as evidenced in Figure S12). The GP/VGSs-CoFe LDH sample reaches a high current density of 2 A/cm² at overpotential of 466 mV (presenting a better Tafel slope of 50 mV/dec). With Pr_6O_{11} anchoring, the GP/VGSs-CoFe LDH-Pr_6O_{11} achieves better OER activity and attains high current densities more easily. The GP/VGSs-CoFe LDH-Pr_6O_{11} electrocatalyst requires only overpotential of 391 mV to achieve a high current density of 2 A/cm² (besides, 311 mV to 500 mA/cm² and 336 mV to 1 A/cm²), meanwhile the corresponding Tafel slope is further reduced to 46 mV/dec. Although the commercial RuO_2 catalyst has a low onset overpotential, its OER catalytic performance in high current density is very poor (reaching only 140 mA/cm² at 1.7 V) with a high Tafel slope of 141 mV/dec. The performance of RuO_2 in high-current-density OER is far inferior to that of our GP/VGSs-CoFe LDH-Pr_6O_{11}.

The VGSs are few-layer graphene that overcome the stacking effect of traditional graphene, offering high electrical conductivity and faster electron transfer pathways

due to their few-layer structure. The VGSs are commonly used as catalyst supports for enhancing the catalytic performance when VGSs combined with metal electrocatalysts. Carbon supports alone typically exhibit low electrocatalytic activity, and carbon substrates grown with VGSs also generally show similar low electrocatalytic activity. This is because the catalytic active species primarily come from the metal catalysts rather than the carbon materials. Thus, the electrocatalytic performance of GP and GP/VGSs exhibits similar low electrocatalytic activity due to the solely composition of carbon without catalytic metal active species. The similar phenomena and the role of VGSs during the electrocatalytic process have been reported in previous reports [25, 26].

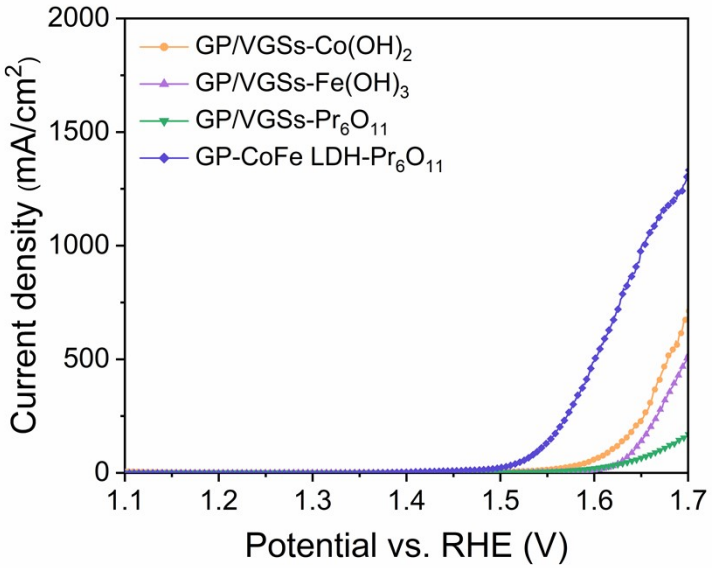

Figure S13. The LSV curves of GP/VGSs-$Co(OH)_2$, GP/VGSs-$Fe(OH)_3$, GP/VGSs-Pr_6O_{11} and GP-CoFe LDH-Pr_6O_{11} in 1 M KOH solution.

When GP/VGSs (as aforementioned poor OER activity in Figure S12) is loaded with metal catalysts such as $Co(OH)_2$, $Fe(OH)_3$ and Pr_6O_{11}, the OER activity is rapidly enhanced. As shown in Figure S13, the GP/VGSs-$Co(OH)_2$ and GP/VGSs-$Fe(OH)_3$ samples can reach current densities of 688 mA/cm² and 510 mA/cm² at 1.7 V (overpotential of 470 mV), respectively, benefiting from the excellent OER activity of Co- and Fe-based catalytic active sites. Moreover, GP/VGSs-Pr_6O_{11} only achieves a current density of 165 mA/cm² at 1.7 V, indicating that rare-earth catalysts alone are less effective in promoting OER activity. For the GP substrate with none of VGSs, the GP-CoFe LDH-Pr_6O_{11} sample only reaches a current density of 1324 mA/cm² at 1.7 V. By comparing it with GP/VGSs-CoFe LDH-Pr_6O_{11} (aforementioned in Figure S12), it is indicated that VGSs provide more loading sites for the electrocatalyst, helping the catalyst achieve higher current density in OER process.

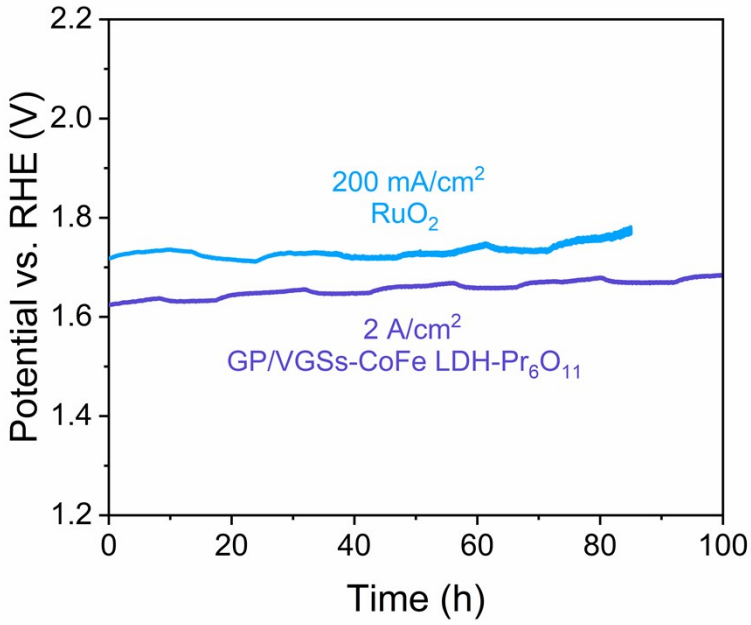

Figure S14. The chronopotentiometric stability test of RuO_2 at a current density of 200 mA/cm^2 and GP/VGSs-CoFe LDH-Pr_6O_{11} at a current density of 2 A/cm^2 in 1 M KOH solution.

As shown in Figure S14, our synthesized GP/VGSs-CoFe LDH-Pr_6O_{11} demonstrates superior OER stability (100 h at a 2 A/cm^2) to the commercial RuO_2 (85 h at 200 mA/cm^2).

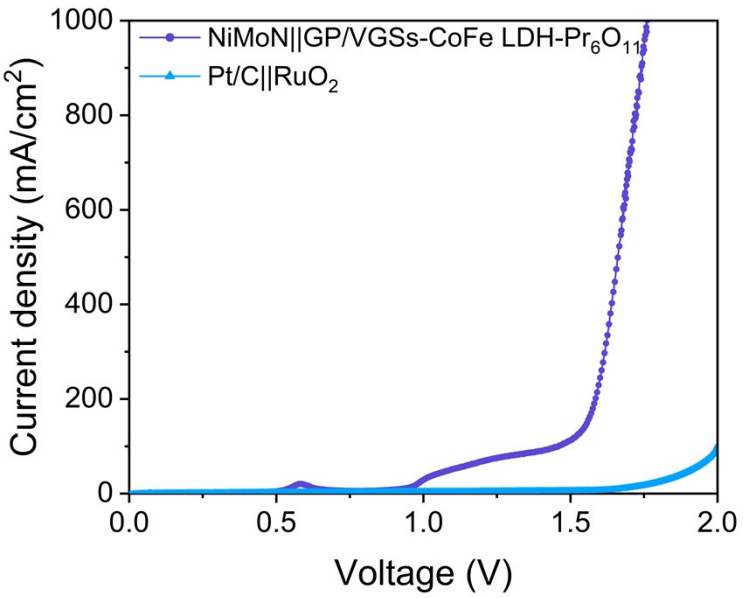

Figure S15. The overall freshwater electrolysis activity of NiMoN||GP/VGSs-CoFe LDH-Pr_6O_{11} and Pt/C||RuO_2 in 1 M KOH solution.

As seen in Figure S15, the NiMoN||GP/VGSs-CoFe LDH-Pr_6O_{11} requires only 1.76 V to obtain a high current density of 1 A/cm². In contrast, commercial RuO_2||Pt/C only reaches a current density of 96 mA/cm² at a voltage of 2 V.

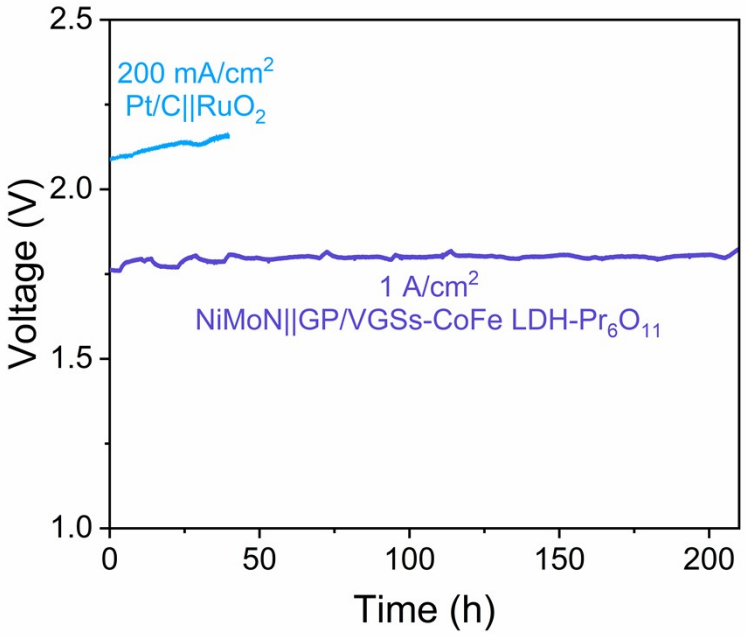

Figure S16 The chronopotentiometric stability test of NiMoN||GP/VGSs-CoFe LDH-Pr_6O_{11} at a current density of 1 A/cm^2 and Pt/C||RuO_2 at a current density of 200 mA/cm^2 in 1 M KOH solution.

As depicted in Figure S16, the NiMoN|| GP/VGSs-CoFe LDH-Pr_6O_{11} stably operates for 210 h at 1 A/cm², which surpasses RuO_2||Pt/C in both current density and stability (40 h at 200 mA/cm²).

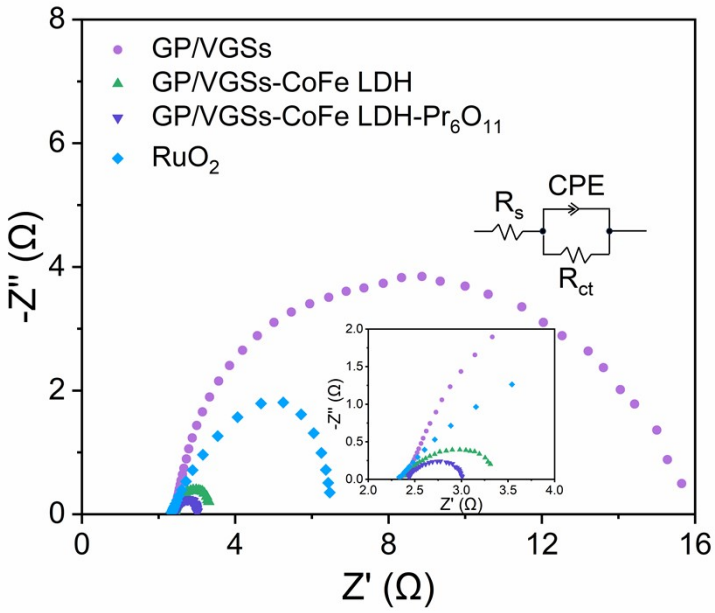

Figure S17. The Nyquist plots and the inset: the corresponding plots at the starting position of GP/VGSs, GP/VGSs-CoFe LDH, GP/VGSs-CoFe LDH-Pr_6O_{11} and RuO_2 in 1 M KOH solution.

The EIS results (Figure S17) imply that GP/VGSs, RuO_2, GP/VGSs-CoFe LDH and GP/VGSs-CoFe LDH-Pr_6O_{11} samples progressively possess lower charge transfer resistance (R_{ct}). The GP/VGSs-CoFe LDH-Pr_6O_{11} sample shows the lowest R_{ct} value of 0.6 Ω, which is 60% of that of GP/VGSs-CoFe LDH sample (1 Ω). The lower R_{ct} value indicates faster electron transfer capability during the OER process, suggesting that the introduction of Pr_6O_{11} onto CoFe LDH enhances the OER kinetics.

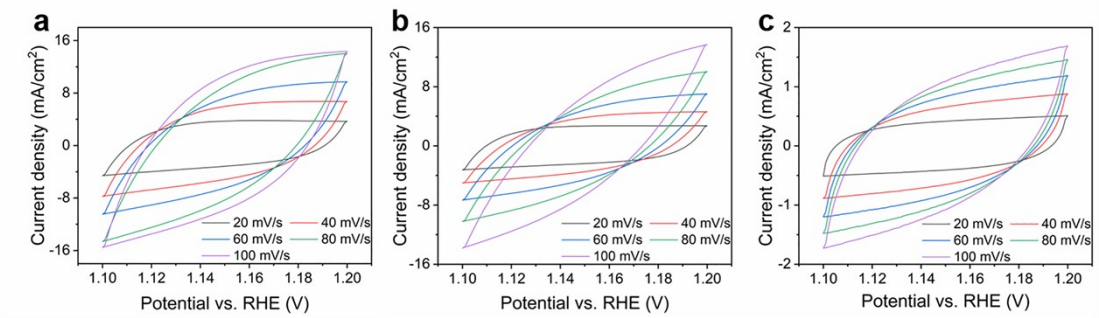

Figure S18. The CV curves of (a) GP/VGSs; (b) GP/VGSs-CoFe LDH and (c) GP/VGSs-CoFe LDH-Pr_6O_{11} at different scan rates in 1 M KOH solution.

The CV curves at scan rates from 20 mV/s to 100 mV/s (Figure S17) are measured in non-Faradaic region for further calculating the C_{dl} values.

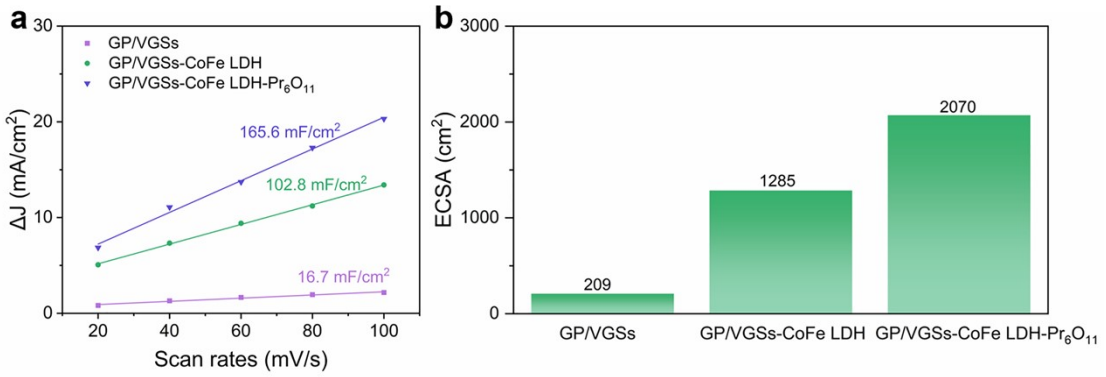

Figure S19. (a) The capacitive current at 1.15 V versus the scan rate and corresponding C_{dl} values and (b) the corresponding ECSA of GP/VGSs, GP/VGSs-CoFe LDH and GP/VGSs-CoFe LDH-Pr_6O_{11}.

The GP/VGSs-CoFe LDH-Pr_6O_{11} presents a highest C_{dl} value of 165.6 mF/cm² (Figure S19a). The ECSA is proportional to C_{dl} for the same type of catalyst [27]. As seen in Figure S19b, the highest ECSA (2070 cm^2) of GP/VGSs-CoFe LDH-Pr_6O_{11} among the three confirm the best catalytic activity.

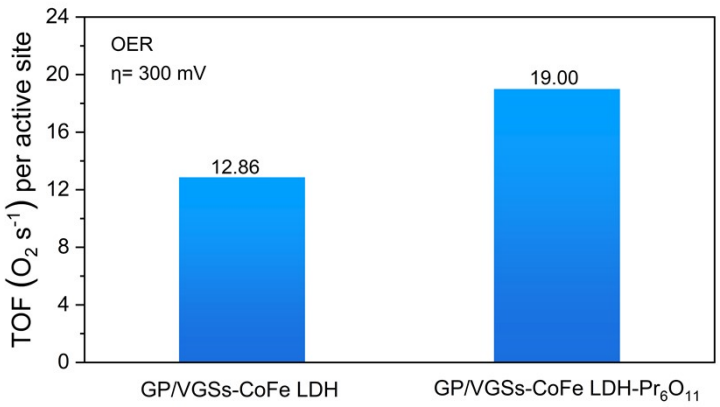

Figure S20. TOF values of GP/VGSs-CoFe LDH and GP/VGSs-CoFe LDH-Pr_6O_{11} for OER at the overpotential of 300 mV in 1 M KOH solution.

As displayed in Figure S20, the GP/VGSs-CoFe LDH-Pr_6O_{11} presents a higher value of 19.00 s^{-1} than GP/VGSs-CoFe LDH (12.86 s^{-1}), which supports the superior OER catalytic activity.

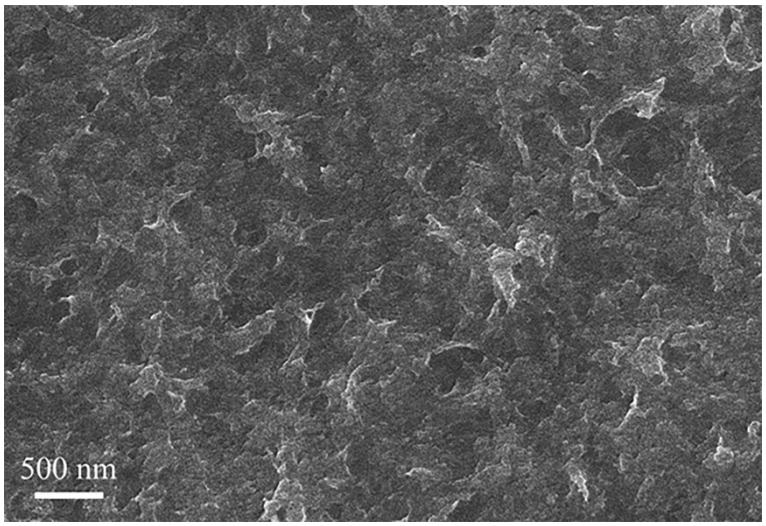

Figure S21. The SEM image of GP/VGSs-CoFe LDH-Pr_6O_{11} after OER long-term process.

Compared SEM images of Figure S21 with Figure S4c, the surface morphology of GP/VGSs-CoFe LDH-Pr_6O_{11} remains essentially unchanged, implying the structural stability of the catalyst.

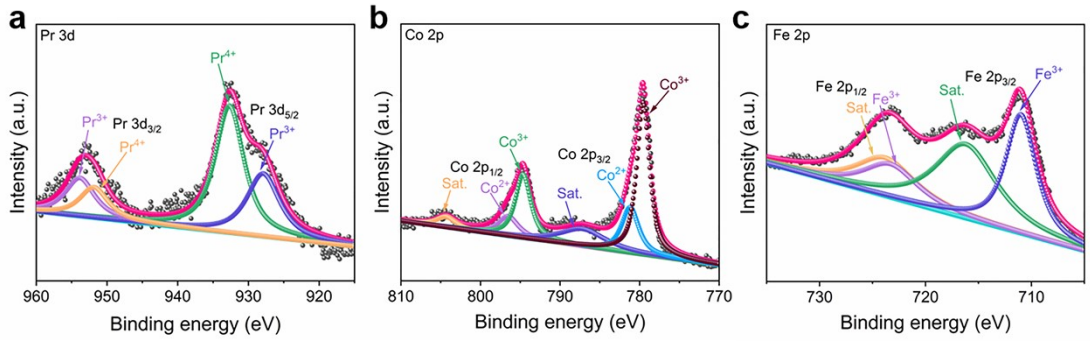

Figure S22. The (a) Pr 3d; (b) Co 2p and (c) Fe 2p XPS spectra of GP/VGSs-CoFe LDH-Pr_6O_{11} after OER long-term process.

Compared XPS results of Figure 2g and Figure S6c-d with Figure S22, it can be seen that characteristic peaks of Pr 3d, Co 2p and Fe 2p are close to the pristine binding energy positions and the peak intensities of Pr^{4+}, Co^{3+} and Fe^{3+} are higher. It indicates that Pr, Co and Fe components of the GP/VGSs-CoFe LDH-Pr_6O_{11} sample can remain well but undergo a certain degree of inevitable oxidation during the OER process.

Table S1. The summary of specific surface area values of GP, GP/VGSs, GP/VGSs-CoFe LDH and GP/VGSs-CoFe LDH-Pr_6O_{11}.

Sample	Specific surface area (m^2/g)
GP	0.561
GP/VGSs	0.920
GP/VGSs-CoFe LDH	0.584
GP/VGSs-CoFe LDH-Pr_6O_{11}	0.880

The VGSs and all metal catalysts are formed in small amounts on the surface of the bulk solid graphite plate (GP). The GP, as the substrate, constitutes the vast majority of the mass and the specific surface area of the GP itself is very low. Therefore, all the synthesized electrocatalysts possess very small specific surface area. The similar phenomenon has also been reported in the literature [28]. For the morphology of GP/VGSs-CoFe LDH (Figure S4b), the surface is composed of sheets with a few hundred nanometers in size. In contrast, the nanosheets on the surface of GP/VGSs-CoFe LDH-Pr_6O_{11} are smaller (Figure 2c, Figure S4c and Figure S7). Therefore, the incorporation of Pr_6O_{11} increases the specific surface area, which corresponds to the experimental result that GP/VGSs-CoFe LDH-Pr_6O_{11} has many finer and smaller nanosheets on the surface.

Table S2. Overall seawater electrolysis activity and durability of NiMoN||GP/VGSs-CoFe LDH-Pr_6O_{11} and recently reported overall electrocatalysts in alkaline seawater.

Electrocatalyst	Current density (mA/cm^2) at 1.7 V	Current density (mA/cm^2) at 1.8 V	Stability	Reference
NiMoN||GP/VGSs-CoFe LDH-Pr_6O_{11}	**326**	**585**	**1 A/cm^2@180 h** **600 mA/cm^2@380 h**	**This work**
RuMoNi||RuMoNi	~250	~400	500 mA/cm^2@240 h	*Nat Commun.* 2023, 14, 3607[29].
CoC_2O_4@MXene||CoC_2O_4@MXene	~80	/	10 mA/cm^2@30 h	*Nat Commun.* 2022, 13, 5785[30].
Fe-Ni_2Pv||Fe-Ni_2Pv	~200	~520	200 mA/cm^2@100 h	*Adv. Mater.* 2024, 36, 2307395[31].
Mo_3Se_4-NiSe||RuO_2	~10	~20	10 mA/cm^2@50 h	*Adv. Mater.* 2024, 36, 2305813[32].
Ni-MoN||SSM	~280	~580	500 mA/cm^2@100 h	*Adv. Mater.* 2022, 34, 2201774[33].
$NiS_{2p}S_x$||$NiS_{2p}S_x$	~30	~50	10 mA/cm^2@50 h	*Adv. Energy Mater.* 2023, 13, 2301907[34].
60Fe/NF||NiMo (6 M KOH at 60 °C)	20	40	100 mA/cm^2@20 h	*Adv. Energy Mater.* 2023, 2301921[35].
Cr-Co_XP||Cr-Co_XP	~30	~70	100 mA/cm^2@160 h	*Adv. Funct. Mater.* 2023, 33, 2214081[36].

$ZnP@Ni_2P\text{-}NiSe_2$‖$ZnP@Ni_2P\text{-}NiSe_2$	~50	~150	10 mA/cm^2@30 h	*Adv. Funct. Mater.* 2022, 32, 2113224[37].
$MoNi_4/MoO_{3-x}$‖$NiFeO\text{-}CeO_2$/NF	~250	500	500 mA/cm^2@200 h	*ACS Nano* 2023, 17, 16008[38].

References

1. H. Sun, C. Tian, G. Fan, J. Qi, Z. Liu, Z. Yan, F. Cheng, J. Chen, C.-P. Li and M. Du, *Adv. Funct. Mater.*, 2020, **30**, 1910596.
2. W. Yaseen, M. Xie, B. A. Yusuf, S. Meng, I. Khan, J. Xie and Y. Xu, *Small*, 2024, **20**, 2403971.
3. H. Zheng, T. Yin, J. Yu, W. Xu, W. Zhang, Q. Yu, Y. Guo, L. Guan, X. Huang and F. Wang, *J. Mater. Chem. A*, 2024, Advance Article, https://doi.org/10.1039/D4TA06305H.
4. J. García-Fayos, R. Ruhl, L. Navarrete, H. J. M. Bouwmeester and J. M. Serra, *J. Mater. Chem. A*, 2018, **6**, 1201-1209.
5. W. Wang, H. Li, C. Y. R. Vera, J. Lin, K.-Y. Park, T. Lee, D. Ding and F. Chen, J. *Mater. Chem. A*, 2023, **11**, 9039-9048.
6. N. Jiang, X. Zhou, Y.-F. Jiang, Z. Zhao, L.-B. Ma, C.-C. Shen, Y. Liu, C.-Z. Yuan, S. Sahara and A.-W. Xu, *RSC Adv.*, 2018, **8**, 17504-17510.
7. G. Zhang, Z. Li, J. Zeng, L. Yu, C. Zuo, P. Wen, Y. Liu, L. Zhong, H. Chen and Y. Qiu, *Appl. Catal., B*, 2022, **319**, 121921.
8. Z. Li, Y. Zhou, M. Xie, H. Cheng, T. Wang, J. Chen, Y. Lu, Z. Tian, Y. Lai and G. Yu, *Angew. Chem. Int. Ed*., 2023, **62**, e202217815.
9. L. Yu, Q. Zhu, S. Song, B. McElhenny, D. Wang, C. Wu, Z. Qin, J. Bao, Y. Yu, S. Chen and Z. Ren, *Nat. Commun*., 2019, **10**, 5106.
10. W. Huo, S. Wang, F. J. Dominguez-Gutierrez, K. Ren, L. Kurpaska, F. Fang, S. Papanikolaou, H. S. Kim and J. Jiang, *Mater. Res. Lett*., 2023, **11**, 713-732.
11. Y. Li, D. Bahamon, M. Sinnokrot and L. F. Vega, *Int. J. Hydrogen Energy*, 2023, **48**, 9700-9712.
12. V. I. Anisimov, I. V. Solovyev, M. A. Korotin, M. T. Czyżyk and G. A. Sawatzky, *Phys. Rev. B*, 1993, **48**, 16929-16934.
13. G. Chen, R. Gao, Y. Zhao, Z. Li, G. I. N. Waterhouse, R. Shi, J. Zhao, M. Zhang, L. Shang, G. Sheng, X. Zhang, X. Wen, L. Wu, C. Tung and T. Zhang, *Adv. Mater.*, 2018, **30**, 1704663.

14. K. L. Yao, Z. B. Li and Z. L. Liu, *J. Magn. Magn. Mater.*, 2008, **320**, 222-226.
15. T. Teusch and T. Klüner, *J. Phys. Chem. C*, 2019, **123**, 28233-28240.
16. J. K. Nørskov, J. Rossmeisl, A. Logadottir, L. Lindqvist, J. R. Kitchin, T. Bligaard, and H. Jónsson, *J. Phys. Chem. B*, 2004, **108**, 17886-17892.
17. L. Wu, L. Yu, F. Zhang, D. Wang, D. Luo, S. Song, C. Yuan, A. Karim, S. Chen and Z. Ren, *J. Mater. Chem. A*, 2020, **8**, 8096-8103.
18. X. Wang, Y. Tuo, Y. Zhou, D. Wang, S. Wang and J. Zhang, *Chem. Eng. J.*, 2023, **403**, 126297.
19. H. Xu, B. Wang, C. Shan, P. Xi, W. Liu and Y. Tang, *ACS Appl. Mater. Interfaces*, 2018, **10**, 6336-6345.
20. Y. Liao, R. He, W. Pan, Y. Li, Y. Wang, J. Li and Y. Li, *Chem. Eng. J.*, 2023, **464**, 142669.
21. M. Gao, X. Wang, M. Z. Afzal, S. Wang and X. Wang, *ChemistrySelect*, 2018, **3**, 10077-10084.
22. Q. Wu, Y. Huang and J. Yu, *Energy Fuels*, 2023, **37**, 19156-19165.
23. S. Hou, A. Zhang, Q. Zhou, Y. Wen, S. Zhang, L. Su, X. Huang, T. Wang, K. Rui, C. Wang, H. Liu, Z. Lu and P. He, *Nano Res.*, 2023, **16**, 6601-6607.
24. Y. S. Park, F. Liu, D. Diercks, D. Braaten, B. Liu and C. Duan, *Appl. Catal., B*, 2022, **318**, 121824.
25. S. B. Roy, S.-K. Jerng, K. Akbar, J. H. Jeon, L. Truong, S.-H. Chun, M. J. Noh, J. Lee and Y.-H. Kim, *J. Mater. Chem. A*, 2019, **7**, 17046-17052.
26. X. Ji, Y. Lin, J. Zeng, Z. Ren, Z. Lin, Y. Mu, Y. Qiu and J. Yu, *Nat. Commun.*, 2021, **12**, 1380.
27. Y. Yoon, B. Yan and Y. Surendranath, *J. Am. Chem. Soc.*, 2018, **140**, 2397-2400.
28. X. Ji, Z. Lin, J. Zeng, Y. Lin, Y. Mu, S. Wang, Z. Ren and Jie Yu, *Carbon*, 2020, **158**, 394-405.
29. X. Kang, F. Yang, Z. Zhang, H. Liu, S. Ge, S. Hu, S. Li, Y. Luo, Q. Yu, Z. Liu, Q. Wang, W. Ren, C. Sun, H. Cheng and B. Liu, *Nat. Commun.*, 2023, **14**, 3607.
30. L. Wang, Y. Hao, L. Deng, F. Hu, S. Zhao, L. Li and S. Peng, *Nat. Commun.*, 2022, **13**, 5785.

31. X. Liu, Q. Yu, X. Qu, X. Wang, J. Chi and L. Wang, *Adv. Mater.*, 2024, **36**, 2307395.
32. M. B. Poudel, N. Logeshwaran, S. Prabhakaran, A. R, Kim, D. H. Kim and D. J. Yoo, *Adv. Mater.*, 2024, **36**, 2305813.
33. L. Wu, F. Zhang, S. Song, M. Ning, Q. Zhu, J. Zhou, G. Gao, Z. Chen, Q. Zhou, X, Xing, T. Tong, Y. Yao, J. Bao, L. Yu, S. Chen and Z. Ren, *Adv. Mater.*, 2022, **34**, 2201774.
34. G. Bahuguna and F. Patolsky, *Adv. Energy Mater.*, 2023, **13**, 2301907.
35. Y. Zhuo, D. Liu, L. Qiao, S. Chen, J. Lu, W. Fai IP, H. Pan and Z. Wang, *Adv. Energy Mater.*, 2023, **13**, 2301921.
36. Y. Song, M. Sun, S. Zhang, X. Zhang, P. Yi, J. Liu, B. Huang, M. Huang and L. Zhang, *Adv. Funct. Mater.*, 2023, **33**, 2214081.
37. K. Chang, D. T. Tran, J. Wang, S. Prabhakaran, D. H. Kim, N. H. Kim and J. H. Lee, *Adv. Funct. Mater.*, 2022, **32**, 2113224.
38. H. Zhang, Z. Bi, P. Sun, A. Chen, T. Wågberg, X. Hu, X. Liu, L. Jiang and G. Hu, *ACS Nano*, 2023, **17**, 16008-16019.